Dynamic crack propagation in weak snowpack layers: Insights from high-resolution, high-speed photography

Bastian Bergfeld[1], Alec van Herwijnen[1], Benjamin Reuter[2], Grégoire Bobillier[1], Jürg Dual[3] and Jürg Schweizer[1]

[1] WSL Institute for Snow and Avalanche Research SLF, Davos, Switzerland
[2] Météo-France, CNRS, CNRM, Centre d'Etudes de la Neige, Grenoble, France
[3] Institute for Mechanical Systems, ETH Zurich, Zurich, Switzerland

Correspondence to: Bastian Bergfeld (bastian.bergfeld@slf.ch)

Abstract. Dynamic crack propagation in snow is of key importance for avalanche release. Nevertheless, it has received very little experimental attention. With the introduction of the Propagation Saw Test (PST) in the mid-2000s, a number of studies have used particle tracking analysis of high-speed video recordings of PST experiments to study crack propagation processes in snow. However, due to methodological limitations, these studies provided limited insight into dynamical processes such as the evolution of crack speed within a PST or the touchdown distance, i.e. the length from the crack tip to the trailing point where the slab comes to rest on the crushed weak layer. To study such dynamical effects, we recorded PST experiments using a portable high-speed camera with a horizontal resolution of 1280 pixels at rates up to 20,000 frames per second. We then used digital image correlation (DIC) to derive high-resolution displacement and strain fields in the slab, weak layer, and substrate. The high frame rates enabled us to calculate time derivatives to obtain velocity and acceleration fields. We demonstrate the versatility and accuracy of the DIC method by showing measurements from three PST experiments, resulting in slab fracture, crack arrest and full propagation. We also present a methodology to determine relevant characteristics of crack propagation, namely the crack speed ($20 - 30$ m s^{-1}), its temporal evolution along the column and touchdown distance (2.7 m) within a PST, and the specific fracture energy of the weak layer ($0.3 - 1.7$ J m^{-2}). To estimate the effective elastic modulus of the slab and weak layer as well as the weak layer specific fracture energy we used a recently proposed mechanical model. A comparison to already established methods showed good agreement. Furthermore, our methodology provides insight into the three different propagation results found with the PST and reveals intricate dynamics that are otherwise not accessible.

1 Introduction

Snow avalanches are among the most prominent natural hazards that threaten infrastructure and people in mountain regions (Pudasaini and Hutter, 2007; Schweizer et al., 2021). While avalanches come in many different types and sizes, here we focus on dry-snow slab avalanches, as these are typically the most dangerous (McClung and Schaerer, 2006). Dry-snow slab avalanche release is the result of a sequence of fracture processes. Failure initiation induced by external loading or the coalescence of sub-critical failures can lead to a localized crack of critical size such that rapid crack propagation starts (onset

of crack propagation) and the slab-weak layer system becomes unstable. In the subsequent dynamic crack propagation phase, the crack self-propagates across the slope without requiring additional load beside the load applied by the slab. Avalanche release then occurs if the gravitational pull on the slab overcomes frictional resistance to sliding, initiating cracks at the crown, flank and stauchwall of the forming avalanche (Schweizer et al., 2003).

35 While avalanche release is a large scale process (slope scale, up to several hundreds of meters), the process zones of the preceding fractures occur on a much smaller scale (snowpack scale, centimetre to decimetre; Sigrist et al., 2005). At the small scale, the snowpack consists of layers with specific mechanical properties related to their complex and often anisotropic microstructure (Walters and Adams, 2014). Studying fracture processes related to avalanche release thus requires experiments large enough to relate to slope scale processes, while also detailed enough to resolve processes at the snowpack scale.

40 Quantities of particular interest during self-sustained crack propagation are the speed of the propagating crack, the touchdown distance, which is the length from the crack tip to the trailing point where the slab rests on the crushed weak layer, and the specific fracture energy of the weak layer (e.g., Schweizer et al., 2011; van Herwijnen et al., 2016b; van Herwijnen et al., 2010).

During the dynamic crack propagation phase, self-sustaining cracking of the weak layer may arrest. It is generally assumed
45 that crack arrest occurs due to spatial variations in snowpack properties. When the weak layer is locally stronger, or the slab thinner, the energy required to extend the crack in the weak layer can be larger than that released during crack extension (Jamieson and Johnston, 1992). If these local disturbances are of small extent, the kinetic energy of the slab can overcome this energy deficit and maintain crack propagation (Broberg, 1996). High crack propagation speeds, resulting in more kinetic energy, may thus favour widespread crack propagation and result in the release of larger avalanches. Despite the importance
50 of crack speed (Gross and Seelig, 2001), very few direct measurements have been made, in particular over distances larger than a couple of meters. High-speed photography of the Propagation Saw Test (PST), a fracture mechanical field experiment for snow (Gauthier and Jamieson, 2006a; Sigrist et al., 2006), combined with Particle Tracking Velocimetry (PTV) provided new insight into weak layer fracture and crack propagation (Schweizer et al., 2011; van Herwijnen et al., 2016a; van Herwijnen et al., 2016b; van Herwijnen et al., 2010). Results highlighted a progressive settlement of the slab during weak layer fracture
55 and compaction (van Herwijnen and Jamieson, 2005; van Herwijnen and Heierli, 2010). Crack propagation speeds derived using threshold values for slope normal displacement range from 10 to 50 m s^{-1} (Bair et al., 2014; van Herwijnen and Jamieson, 2005; van Herwijnen and Birkeland, 2014; van Herwijnen et al., 2016). Therefore, speeds are in line with theoretical predictions of incipient shear cracks (McClung, 2005) and asymptotic flexural speeds (Heierli et al., 2008b). A comparison to an alternative experimental technique deriving crack speeds in PSTs is missing, but needed since the current methodology
60 assumes that collapse is in line with crack advance. An increase in crack speed with increasing slab density and increasing collapse height was observed (van Herwijnen and Birkeland, 2014; van Herwijnen and Jamieson, 2005).

Experimental data on the touchdown distance are very limited. Bair et al. (2014) were the only to report experimentally estimated touchdown distances. These ranged from 2.5 to 3.3 m (for slab densities ranging from 197 to 249 kg m^{-3} and slab thicknesses between 0.45 and 0.58 m) and were therefore twice as large as what was predicted with the model of Heierli (2008).

65   To determine weak layer specific fracture energy w_f different methodologies exist, yielding results comparable to the specific fracture energy reported for opening cracks in solid ice (tensile loading). Thus, one might conclude that the reported values for snow are not realistic. However, experimentally obtained fracture parameters are always related to the applied loading condition. In other words, the fracture energy for a Mode I and a Mode II crack are different material properties, the same accounts for specific fracture energies measured in compressional and tensional loading experiments. Both energies are

70 independent material properties, although both are considered as Mode I (Alfarah et al., 2017; Heierli et al., 2012). For snow, specific fracture energies were mostly obtained with PST experiments, hence in mixed-mode (compression-shear) loading, typically with the compressive part dominating. A comparison to the compressive specific fracture energy of solid ice would therefore be more appropriate, yet such values are not reported in the literature. Sigrist and Schweizer (2007) were the first to estimate w_f for snow (mean 0.07 J m^{-2}), combining field experiments with finite element (FE) modelling. Their method used

75 the critical cut length from a PST and snow micro-penetrometer measurements (SMP; Schneebeli and Johnson, 1998) to estimate the effective elastic modulus of the slab. Using the same approach, Schweizer et al. (2011) reported values an order of magnitude larger, typically around 1 J m^{-2}. This discrepancy was in part attributed to lower estimates of the slab effective modulus resulting from different signal processing method for SMP force signals (Löwe and van Herwijnen, 2012; Marshall and Johnson, 2009). This demonstrates a weakness of the method, as the back-calculated specific fracture energy relies on the

80 input of the elastic modulus, a property that cannot easily be measured and introduces large uncertainties. To resolve this discrepancy, van Herwijnen et al. (2016) presented a field-based experimental approach to simultaneously determine the effective elastic modulus and the specific fracture energy. They reported values for the specific fracture energy ranging from 0.08 to 2.7 J m^{-2}. Similar values (0.5 and 2 Jm^{-2}) were also found by integrating the SMP penetration force signal over the weak layer thickness (Reuter et al., 2015; Reuter et al., 2019). Hence, there is no single method available to derive consistent

85 values of the important metrics describing crack propagation.

    The aim of the present work is to introduce a field applicable method to investigate the dynamics of crack propagation and derive characteristic measures of crack propagation such as speed, touchdown distance and specific fracture energy. To this end, we employed a portable high-speed camera (up to 20,000 frames per second) and recorded densely speckled flanks (or side walls) of PST experiments. These sequences of images were then used to perform digital image correlation (DIC),

90 providing full-field displacement and strain fields. We show results from three flat field PST experiments that resulted in slab fracture (SF), crack arrest (ARR) or crack propagation until the far end of the column (END). For the latter, we evaluated crack speed evolution along the PST column from slab displacement as well as from alternative methods based on slab acceleration or weak layer strain. Finally, the touchdown distance was estimated from the downward slab velocity, and we computed weak layer specific fracture energy as well as weak layer and slab elastic modulus from the displacement field of the slab.

2.   Methods

We performed fracture mechanical field experiments based on the Propagation Saw Test (PST) design on three measurement days on a flat and uniform site close to Davos, Switzerland. Using high-speed videos of the experiments, we applied digital image correlation (DIC) to derive high-resolution displacement and strain fields of the slab, weak layer and substrate.

2.1. Field measurements

On each of the three measurement days, we performed a PST. This is a standard fracture mechanical test for snow (Gauthier and Jamieson, 2006b; Sigrist and Schweizer, 2007) whereby a 30 cm wide column is isolated and an artificial cut is introduced within a weak snow layer until, at the critical cut length r_c, a self-propagating crack starts. Unlike the standard PST guidelines (Greene et al., 2016), recommending a column length of 120 cm, our PSTs were at least 230 cm long.

Close to the PST experiment, we characterized the snowpack with a traditional manual snow profile following Fierz et al. (2009). Density was measured using a 100 cm^3 cylindrical density cutter (38 mm diameter) with a vertical resolution of 5 cm. Spatial variability of the snowpack was assessed with snow micro-penetrometer (SMP) measurements approximately every 50 cm along the PST experiments.

The exposed side wall of the PST was speckled with black ink (Indian Ink, Lefranc & Bourgeois) applied with a commercial garden pump sprayer. Using a high-speed camera (Phantom, VEO710), we filmed the entire speckled wall of the PST experiment with rates up to 20,000 frames per second (fps) and a horizontal resolution of 1280 pixel. We adjusted the vertical resolution for each PST individually to maximize frame rate and recording duration, which is limited by the 18 GB internal memory of the camera. Due to this limitation, we could not always record the full sawing phase prior to rapid crack propagation in the PST experiments. We attached a circular marker to the tip of the 2 mm thick snow saw to determine the location of the saw tip in all frames using particle tracking.
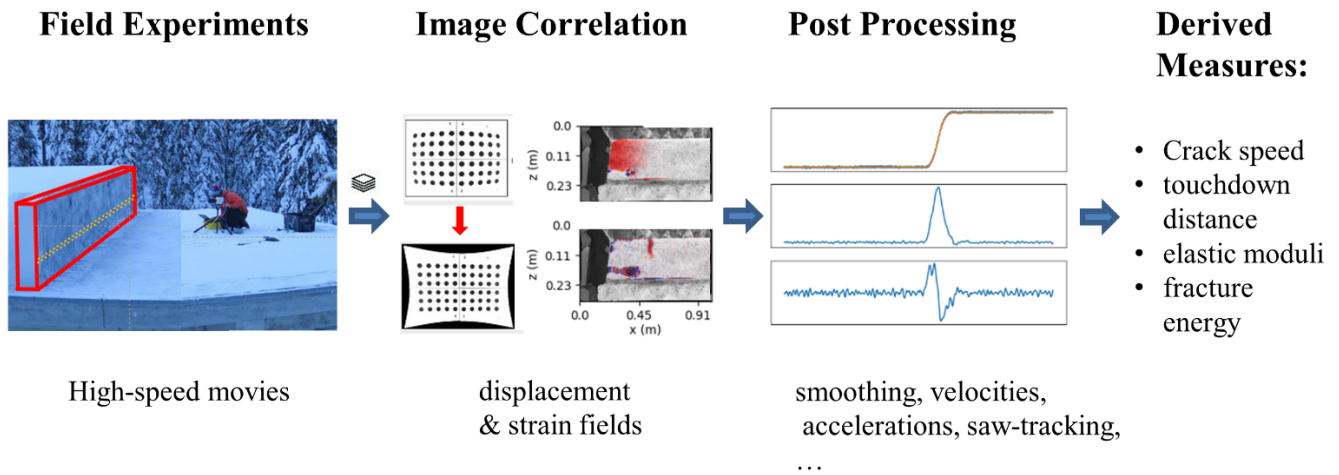
2.2. Image processing

Camera distortion correction

To avoid perspective distortion, we aligned the camera vertically and horizontally perpendicular to the wall, and aimed the optical axis of the camera at the centre of the PST, both horizontally and vertically. To correct for radial and tangential image distortion introduced by the camera lens we used calibration factors using a pinhole camera model. The distortion coefficients k_1, k_2, k_3, p_1, p_2 as well as the camera model were estimated using chessboard calibration images and routines using OpenCV for Python (Bradski and Kaehler, 2008). The distortion coefficients are constant, as these only depend on lens characteristics. In the field, we changed the image resolution to allow for longer recording times and higher frame rates. We thus scaled the camera model matrix accordingly. Camera calibration was performed on the fly while correlating the images with DICengine (Turner, 2015). As a result, black curved borders are introduced in the corrected images (Figure 1)

Digital image correlation

For the digital image correlation (DIC) analysis we used DICengine, an open source software provided by Sandia National Laboratories (Turner, 2015). In the images, a region of interest (ROI) was selected encompassing the speckled PST wall. To derive displacement and strain fields of the PST, the ROI was further subdivided into quadratic DIC subsets with a certain side length and step size (Table 1). The position and deformation of each DIC subset was then tracked over time using the first frame of the movie as a reference. In order to find the unique DIC subsets in all subsequent frames, the DIC subsets were allowed to translate, rotate and deform in normal and shear. For an arbitrary DIC subset i, we thus obtained the initial horizontal and vertical position (x_i, z_i) within the reference image as well as the time (t) dependent horizontal and vertical displacement $u_i(t)$, $w_i(t)$ relative to the initial position, the rotation, normal strain $\varepsilon_{zz,i}(t)$ and shear strain $\varepsilon_{xz,i}(t)$.

Figure 1: Schematic of data processing. After the field experiments were filmed, the frames were analysed using digital image correlation. Displacements obtained with DIC were smoothed to derive velocity and acceleration and thus quantities relevant for crack propagation.

Post processing

Since the DIC output is in image space, we first converted it to real space with units of metres. For this, we manually picked a reference length of 2 m in a reference image taken before the experiment to determine the conversion factor. We also changed the origin and orientation of the coordinate system to the upper left corner of the slab with x positive right and z positive downwards.

In the next step, we divided the ROI into three subregions: (i) slab, (ii) weak layer and (iii) substrate. This was done by drawing an upper and lower boundary of the weak layer manually into the displacement field after fracture. All DIC subsets above the upper boundary were assigned to the slab, all those below the lower boundary to the substrate and all in between to the weak layer.

Since the frame rate of the recorded videos is high compared to crack propagation time, we smoothed the displacements $u_i(t)$, $w_i(t)$ using a 3rd order Savitzky-Golay filter with a window size of 201 frames. To compute velocity and acceleration of the DIC subsets, the first and second derivative of the smoothed displacement curves were taken (Figure 1).

Tracking the saw

When sawing into the weak layer, the location of the saw needs to be known to model the resulting slab deformation. We therefore tracked the dot mounted on the tip of the saw using DICengine's tracking functionality (Turner, 2015). Since the dot was not perfectly aligned with the PST sidewall, camera perspective introduced an offset, which was estimated as the mean difference $\overline{r_{off}} = \frac{1}{n}\Sigma_{frames}(r_{\mathrm{man}\,i} - r_{\mathrm{dot}\,i})$ between the automatically tracked cut length r_{dot} and the manually picked cut length r_{man}. We corrected for this offset by $r = r_{\mathrm{dot}} + \overline{r_{off}}$ (Figure 2b). Uncertainty of the manual picking was estimated to be 3 pixels (Figure 2b, red transparent region). For the uncertainty of the automatic tracking we took 3 times the predicted standard deviation of the tracking solution (not visible in Figure 2b)
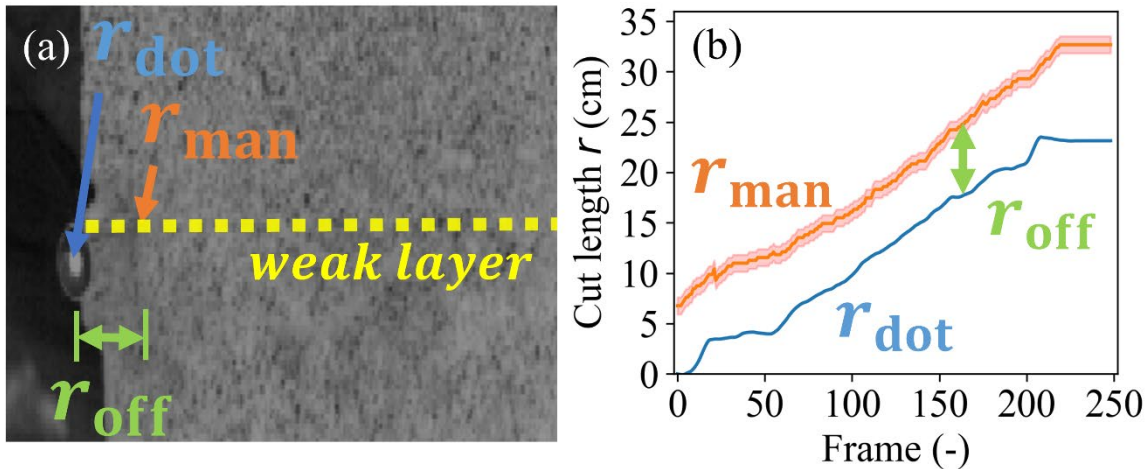
Figure 2: (a) Close up of the saw end of a PST experiment. The saw cut in the weak layer (dashed yellow line) extended to the orange arrow. Due to the camera perspective, the tracked dot on the saw tip (blue arrow) appears at an offset (r_{off}) to the manually estimated saw cut position (r_{man}, orange line in (b)). (b) The offset between the tracked (blue) and the manually picked cut length (orange) was approximately constant over all frames. Uncertainty is depicted as the red transparent region.

2.3. Mechanical properties

To determine the effective elastic modulus of the slab E_{sl} and the weak layer specific fracture energy w_f, a mechanical model is required to fit to the experimental data (e.g., van Herwijnen et al., 2016). We used two different approaches based on the displacement field and one approach based on SMP measurements.

As a first approach, we followed the methodology described by van Herwijnen et al. (2016), based on fitting the equation for the mechanical energy provided by Heierli et al. (2008a). We will call this the "VH" method. van Herwijnen et al. (2016) estimated the effective elastic modulus $E_{\mathrm{sl}}^{\mathrm{VH}}$ of the slab and the weak layer specific fracture energy w_f^{VH} from changes in

mechanical energy $V_m(r)$ with cut length r. Using the theorem of Clapeyron, the mechanical energy $V_m(r) = -\frac{1}{2}V_p(r)$ of the slab is derived from the loss in gravitational potential energy V_p. In our experiments, for a given cut length r, we computed the median z-displacement $<w^r(x)>$ for each column in the slab (DIC subsets with same location x) and summed their contributions to the gravitational potential energy V_p:

$$V_m(r) = -\frac{1}{2}V_p(r) = -\frac{1}{2}\sum_x m\, g < w^r(x) >, \qquad \qquad \mathbf{1}$$

where g is the gravitational acceleration. The column mass per unit width was determined as $m = \Delta SS\, D\, \rho_{slab}$, with ΔSS the DIC subset step size, D slab thickness and ρ_{slab} mean slab density (Table 1). Fitting the expression for the mechanical energy $V_m\left(E_{sl}^{VH}, v_{sl}, D, \rho, \theta, r\right)$ (Heierli et al., 2008a; eqs 1 & 5) to the data, the slab elastic modulus E_{sl}^{VH} can be determined (orange line in Figure 3a). Here, v_{sl} is the Poisson's ratio (assumed to be 0.25) and θ is the slope angle. The specific fracture energy of the weak layer is then obtained by numerical differentiation of the mechanical energy $w_f^{VH} = -\frac{d}{dr}V_m\Big|_{r=r_c}$ at the critical cut length r_c. The latter equation holds, independently of the chosen expression for V_m. The only constraint on V_m is that it is zero at the origin ($r = 0$) and that it decreases monotonically with r. We therefore also fitted a power-law function of the form $f(r) = -ar^b$ to the data (black dashed line in Figure 3a) to provide an alternative estimate of the specific fracture energy w_f^{FU}. To assess the quality of both functions, $V_m(r)$ and $f(r)$, we computed the root mean squared errors, denoted RMSE^{VH} and RMSE^{FU}, respectively.
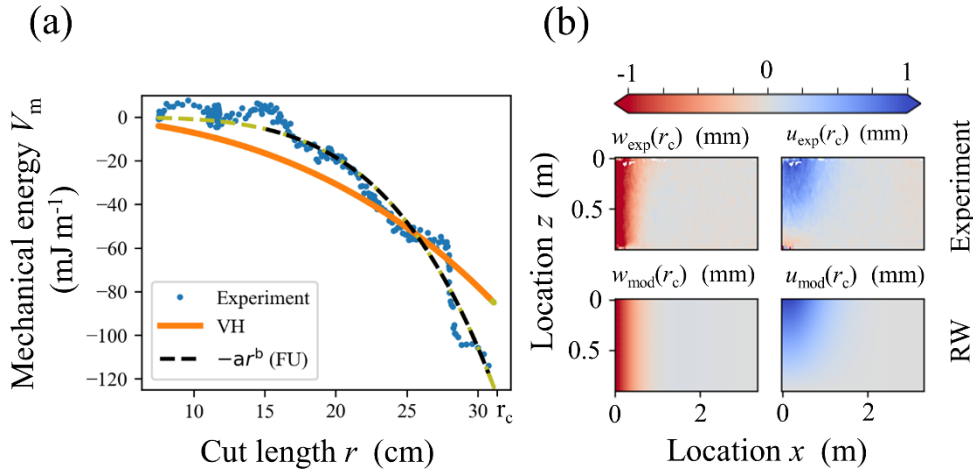

Figure 3: (a) Mechanical energy $V_m(r)$ of the slab as a function of cut length r. The orange line is a fit of the theoretical expression of V_m with slab elastic modulus as a free parameter. The black dashed line is a power-law fit to the data. The green sections of the curve are extrapolations of the fits extend to $r = r_c$, where the derivative is taken to estimate the weak layer specific fracture energy w_f^{VH} and w_f^{FU}. (b) Vertical (w) and horizontal (u) displacement fields at $r = r_c$ in the left and right column, respectively. Measured displacement fields are shown in the top row, while the corresponding modelled displacements using the approach described by Rosendahl and Weissgraeber (2020) are shown in the bottom row.

Second, we used the model suggested by Rosendahl and Weissgraeber (2020), which we will call the "RW" method. Their model considers a Timoshenko beam sitting on a weak layer represented by smeared springs, in contrast to the model of Heierli et al. (2008a), where the weak layer is assumed rigid. The RW model predicts horizontal (along the PST column length l, x-direction) and vertical (along D, z-direction) slab displacements $u(x,z)$ and $w(x,z)$ for different cut lengths r. Required model parameters are the geometrical PST parameters (D, l, θ, column width b and weak layer thickness d), the elastic modulus of the slab(E_{sl}^{RW})and the weak layer (E_{wl}^{RW}), and the Poisson's ratios of the slab (ν_{sl}) and the weak layer (ν_{wl}), both assumed 0.25. To derive E_{sl}^{RW} and E_{wl}^{RW}, we computed a residual ε between the measured (u_{exp}, w_{exp}) and modelled (u_{RW}, w_{RW}) displacements (Figure 3b, top and bottom, respectively):

$$\varepsilon = \sum_{k=0}^{SS} \left| u_{RW}^k\left(E_{sl}^{RW}, E_{wl}^{RW}\right) - u_{exp}^k \right| + \left| w_{RW}^k\left(E_{sl}^{RW}, E_{wl}^{RW}\right) - w_{exp}^k \right|, \qquad \textbf{2}$$

where the sum is over all DIC subsets SS contained in the slab. Then, we used a least squares optimization routine from scipy (Virtanen et al., 2020) to find the optimal set of E_{sl}^{RW} and E_{wl}^{RW}. The weak layer fracture energy w_f^{RW} is obtained by:

$$w_f^{RW} = G_I + G_{II}, \qquad \text{with: } G_I = \frac{E_{wl}^{RW}}{2t} w_{RW}(r = r_c)^2 \text{ and } G_{II} = \frac{E_{wl}^{RW}}{2t(\nu_{wl}-1)} u_{RW}(r = r_c)^2 \qquad \textbf{3}$$

where G_I and G_{II} are the contributions from mode I and mode II, respectively.

As a third approach, we used SMP measurements. The effective elastic modulus E_{sl}^{BR} was derived from SMP data as described by Reuter and Schweizer (2018), using the signal interpretation method suggested by Löwe and van Herwijnen (2012). Reuter et al. (2013) suggested a parametrization of the specific fracture energy based on the penetration resistance $F(z)$. Using a moving window (size: $w = 2.5$ mm) to integrate $F(z)$, they defined the specific fracture energy as the minimum of the integral within the weak layer:

$$w_f^{SMP} = \frac{1}{A} \min_{WL} \int_{-w/2}^{w/2} F\, dz \,, \qquad 4$$

Where A is a fitting parameter. The integration has units of energy (J) and relates to the work required to destroy the snow structure along the integration path. Specific fracture energy, however, has unit energy per area. Therefore, it is necessary to divide by an effective area, the fitting parameter A. While the effective area is unknown, it is likely larger than the cross section of the tip diameter (Johnson, 2003), and depends on snow structure (van Herwijnen, 2013). We therefore followed Reuter et al. (2019), and introduced a fitting parameter A to implicitly account for the unknown effective area. The fitting parameter was derived using a linear regression to PTV derived specific fracture energies (Figure 6 in Reuter et al. (2019)), resulting in $A = 3.4 \times 10^{-4}\, m^2$, which relates to a plausible effective cone area of 3.4 cm^2 (radius $\approx$ 1 cm).

2.4. Crack propagation properties

As characteristics of crack propagation, we computed the temporal evolution of crack speed and touchdown distance for PST experiment #3 (PST3), where the crack travelled to the end of the column.

Crack speed

We investigated three methods to derive crack speed. First, we used a method similar to that described by van Herwijnen and Jamieson (2005). As the crack propagates through the weak layer, the weak layer collapses, and displacement curves of DIC subsets in the slab gradually show settlement (Figure 4a). We used the time delay Δt when the smoothed displacement curves crossed a threshold value of 0.2 mm (the typical standard deviation of w) to determine crack speed (inset in Figure 4a). The time each DIC subset crossed the threshold value was linked to its x-position (blue dots in Figure 4b). Computing the median for all DIC subsets with the same x-location, (orange crosses in Figure 4c), crack speed $c^{\mathrm{disp}} = \Delta x / \Delta t$ was then determined as the slope of linear fits in overlapping moving windows (15 cm, step size 3.4 cm, red line in Figure 4c).
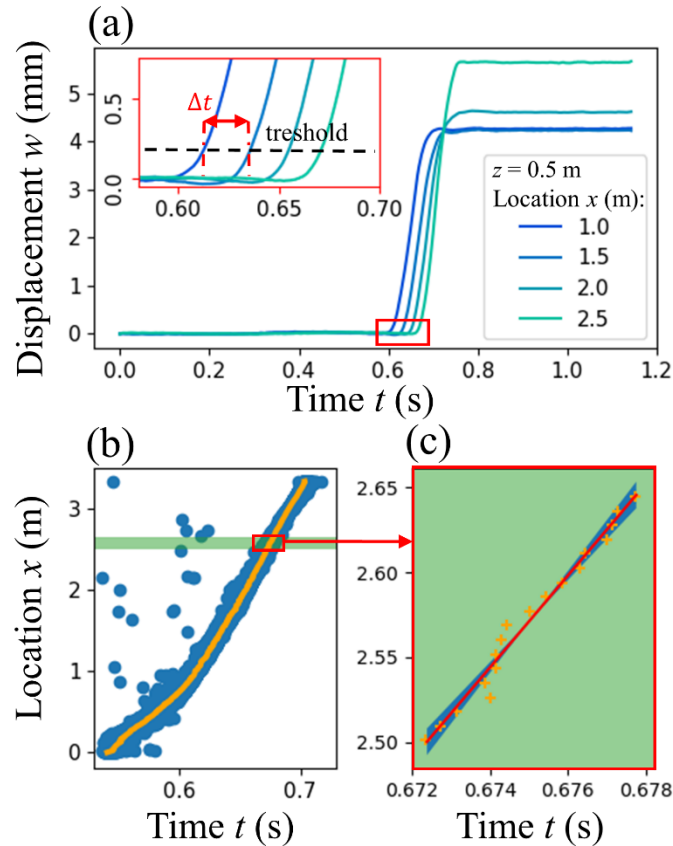

Figure 4: (a) Slope normal displacement with time for four DIC subsets along the PST. Colours indicate the x-location of the DIC subsets. The inset shows the displacement threshold (dotted line) used to determine the time difference Δt between the different DIC subsets. (b) Position of DIC subset with time the threshold was passed. Blue dots show individual DIC subsets while the orange dots show the median of all DIC subsets with the same x-location. (c) Position of DIC subset with median time of threshold crossing (orange crosses) for the green area shown in (b). The red line shows the linear fit used to obtain crack speed. The shaded blue areas show the 95% confidence interval.

Secondly, we used the normal strain from weak layer DIC subsets. Similar to the displacement-based method, we first smoothed the strain curves $\varepsilon_{zz,i}(t)$ (Savietzky-Golay filter, window size 31 DIC subsets and order 3) before applying a threshold

of -0.01 to the strain in the weak layer. We removed outliers by neglecting time stamps below the 5th percentile and above the 95th percentile. For the remaining time stamps, we calculated the median of all DIC subsets with the same x-location before we estimated crack speed c^{strain} as the slope of linear fits to overlapping moving windows (25 cm, step size 2.5 cm).

235 Thirdly, we calculated crack speed by cross-correlating the slope normal acceleration $\ddot{w}(t)$ of the DIC subsets. For a given beam section of width $\Delta x = 30$ cm, we cross-correlated the slope normal acceleration curves $\ddot{w}(t)$ of all DIC subset pairs with same z-location (without repetition) to obtain time lags Δt with pair spacing Δd (Figure 5). Crack propagation speed was then determined by a linear fit for data pairs of time and pair spacing, Δt vs. Δd. Thus, this approach allowed us to obtain a crack speed estimate $c^{\text{corr}}(x)$ for a specific beam section without having to choose a threshold value.

240 For all three methods, the uncertainty in the crack speed values was obtained from the 95 % confidence interval of the fit (e.g. blue region in Figure 4c), and crack speed over the entire PST experiment was taken as the mean of $c(x)$.
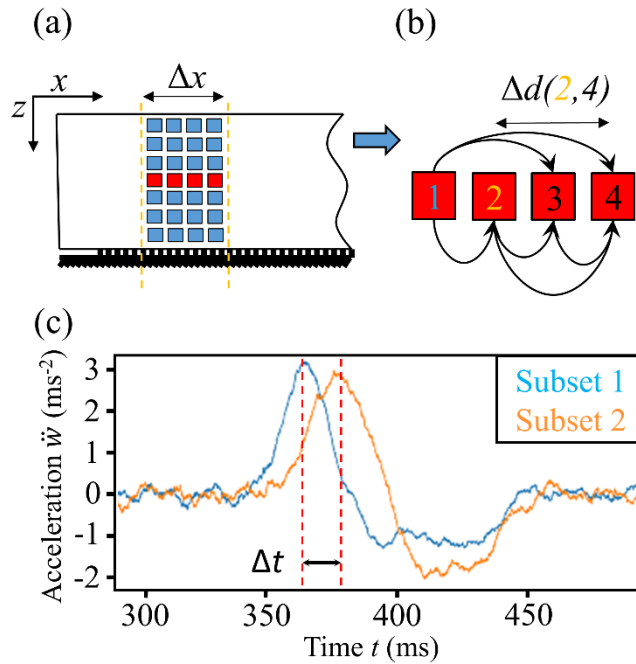
Figure 5: (a) For the correlation-based speed estimation we used beam sections containing vertically and horizontally aligned DIC subsets (squares). **(b)** For a line of DIC subsets (same z-location), all possible combinations of DIC subset pairs with a distinct distance Δd are shown (black arrows). **(c)** By cross-correlating the normal acceleration $\ddot{w}(t)$ of a subset pair, we derived the time lag
245 Δt needed to determine crack speed.

Touchdown distance

As the crack propagates through the PST column, the slab subsides before it comes to rest on the crushed weak layer. As long as a DIC subset in the slab is ahead of the crack tip, it has a slope normal velocity $\dot{w}(t)$ of zero. The velocity then increases as the crack passes underneath. Finally, as the crack has passed, $\dot{w}(t)$ returns to zero. We therefore defined the length λ as the
250 distance between DIC subsets at rest before and after the collapse. To estimate λ, we averaged normal velocities $\dot{w}(t)$ of all vertically aligned DIC subsets in the slab for each time step (coloured lines in Figure 6). Then, we performed spatial smoothing

along x (Savitzky-Golay, window 61, order 3, red dashed lines in Figure 6) before applying a threshold of 1.9×10^{-4} m s^{-1} to $\dot{w}(t)$ (standard deviation before crack propagation). The touchdown distance λ was then defined as the distance over which subsets exceeded the velocity threshold (red arrow in Figure 6). The uncertainty in λ was arbitrarily defined as the difference with the value obtained using a three times larger threshold value for $\dot{w}(t)$.
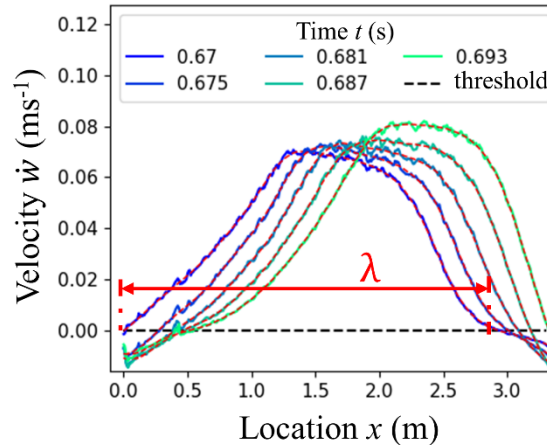

Figure 6: **Raw (solid lines) and smoothed (red dashed lines) vertical velocity $\dot{w}(t)$ of DIC subsets in the slab with x-location for different times during crack propagation. At each time step, the touchdown distance λ was estimated as the distance between the two closest subsets that are at rest, i.e. below the threshold value (black dashed line). The touchdown-distance at time 0.67 s is shown in red.**

3. RESULTS

We analysed three PSTs performed within 10 days in January 2019 at the same site and on the same weak layer consisting of buried surface hoar. We did not note any changes of the weak layer during this period in terms of layer thickness and grain size (Table 1). The thickness of the slab, on the other hand, increased from 23 to 83 cm, the load increased from 318 to 1217 Pa, and mean slab density ranged between 136 and 149 kgm^{-3}. The mean penetration resistance of the slab increased from 90.6 to 220 mN. Overall, the heterogeneity along the three PSTs was negligible and the SMP measurements were in good agreement with manual profiles (e.g. PST3 in Figure 7).

The critical cut length increased from PST1 to PST3 and crack propagation characteristics were very different. Indeed, PST1 resulted in crack arrest due to a slab fracture (SF), PST2 showed crack arrest (ARR) without slab fracture, and in PST3 the crack propagated to the very end of the column: full propagation (END).

11
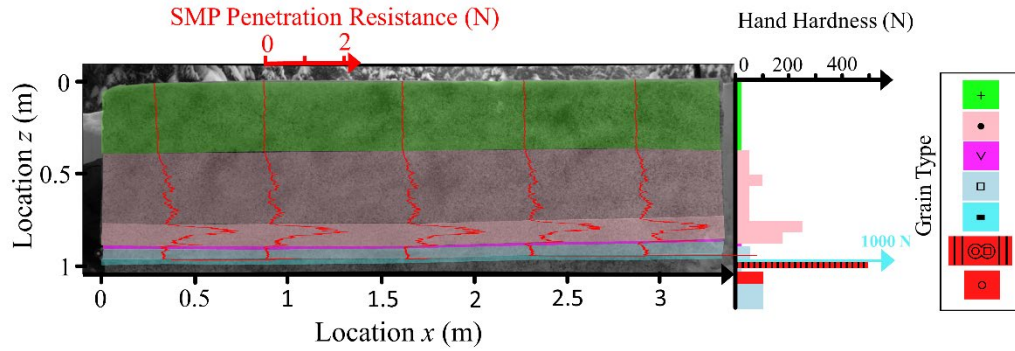
Figure 7: SMP measured penetration resistance (red lines plotted on the PST image) throughout experiment PST3. The colouring of the background corresponds to the layers identified in the manual profile (right side). The manual profile shows hand hardness index and grain shape indicated by colours (Fierz et al., 2009).

Table 1: Overview of experimental parameters, slab and weak layer characteristics from the manual profile and SMP measurements as well as video and DIC analysis parameters for the three flat field PSTs (slope angle 0°).

PST	PST number	1	2	3
	Date	4 Jan 2019	10 Jan 2019	13 Jan 2019
	test result	slab fracture	crack arrest	full propagation
	column length (m)	2.3	3.3	3.3
	critical cut length (m)	0.205	0.22	0.33
slab	slab thickness (m)	0.23	0.565	0.74
	mean slab density (kg m^{-3})	138	136	149
	mean penetration force (mN)	90.6	116.0	220.1
weak	grain type	∨ (SH)	∨ (SH)	∨ (SH)
layer	grain size max (mm)	15	15	15
	grain size avg (mm)	10	10	10
video	frame rate (frames s^{-1})	20,000	14,000	7,000
	image height (pixel)	256	400	400
	lens aperture value	2.8	2.8	2.8
	lens focal length (mm)	24	24	24
DIC	subset size (pixel)	9	12	12
	subset step size ΔSS (pixel)	3	3	3

3.1. Displacement and strain

While visual observation of the PSTs in the field allowed us to detect the outcome of PST1 as SF and PST3 as END, we could not discern the result of PST2. We noticed crack propagation did not reach the far end, without seeing obvious indications of where the crack had stopped. It only became clear after consulting the displacement and strain fields that PST2 had resulted in ARR.

For PST3 (END), $w(t)$ increased with time, starting at the sawing end. Total z-displacement after weak layer fracture was lowest between positions 0.8 m < x < 2 m along the beam. For x > 2 m, the total $w(t)$ increased up to 10 mm – about twice as much as for smaller x. This large $w(t)$ is attributed to a secondary crack propagating in the opposite direction, which is particularly clear in the strain field after crack propagation (Figure 8 c3 and Supplement A for the temporal evolution). This secondary crack propagated when the initial crack in the surface hoar weak layer at $z = 0.8$ m reached the far end of the column. The propagation of this secondary crack is also clearly visible in the x-displacement (Figure 8 c2). For $x < 2$ m, $u(t)$ returned to zero after crack propagation. For $x > 2$ m, on the other hand, a residual positive x-displacement remained after crack propagation (e.g., $t = 0.8$ s). This residual x-displacement is grouped into three sections that align very well with the two slab fractures stopping this reverse propagating crack (Video A1 in the Supplement). While in the field we classified PST3 as END, the displacement and strain data clearly show that the crack propagation dynamics were more intricate, and a combination of END, SF and ARR. This unexpected result was not recognized in the field.

In PST1 the slab fracture (SF) was visible in the field and also clearly reflected in the measurements, most notably in the strain field (Figure 9). When the saw reached $r = 20$ cm, a crack within the weak layer started propagating ($t = 90$ ms in Figure 9 b). A tensile crack in the slab then opened at $x_{SF} = 32$ cm ($t = 120$ ms in Figure 9 c) and stopped crack propagation in the weak layer ($t = 160$ ms in Figure 9 d). As the slab fractured, $w(t)$ left of the SF ($x < x_{SF}$) exhibited downward displacement (positive z) whereas columns very close to x_{SF} show upward displacement (negative $w(t)$, Figure 8 a1). This suggests that the portion of the slab that became detached rotated with a rotation point close to x_{SF}. The x-displacement (mean along z) of all DIC subsets in the detached part of the slab was very similar (blue and green lines in Figure 8 a2).
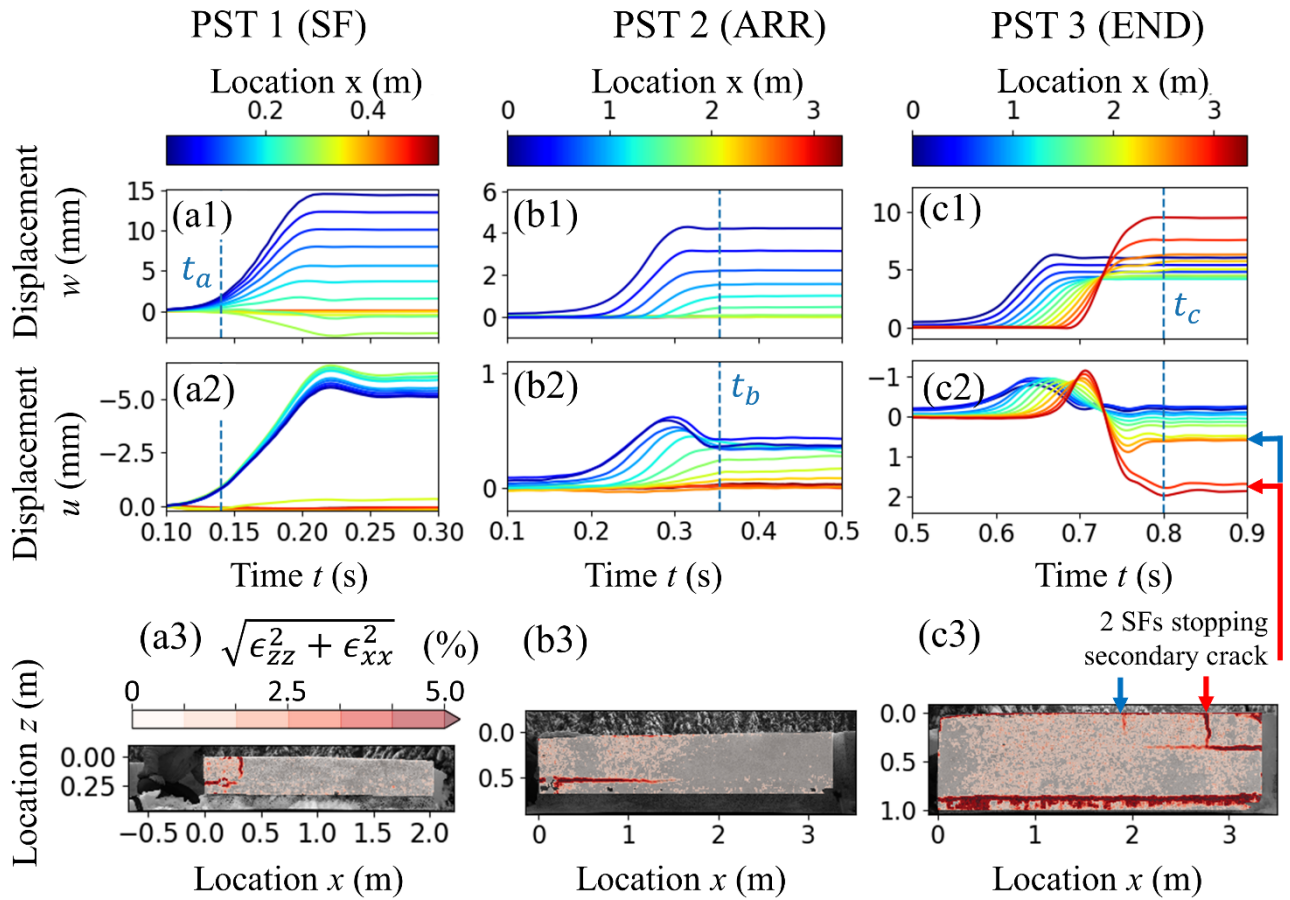
Figure 8: Displacement and strain fields for the three different PSTs. (a) Slab fracture, (b) arrest (c) full propagation. The deformation of the slab with time is shown as displacement curves *w* (vertical, along *z*, first row) and *u* (horizontal, along *x*, second row) measured at various locations *x* along the PST beam (colours). The third row shows the strain fields at the respective times t_a, t_b and t_c, indicated with the dashed lines in the upper two rows. Strain concentration around cracks is clearly visibly.
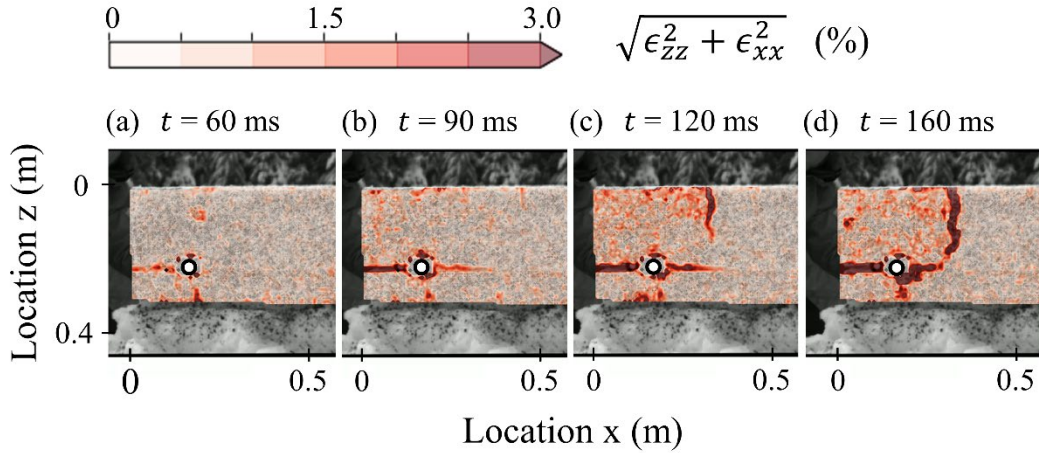
Figure 9: Magnitude of normal strains (colours) in the first half meter of PST1 at four different time steps: (a) no weak layer cracking ahead of the snow saw (black circles with white dot), (b) crack propagation ahead of the saw, (c) appearance of a crack in the slab propagating downwards from the snow surface, and (d) both cracks have merged.

PST2 resulted in crack arrest (ARR) and the strain at time $t = t_b$ at the end of crack propagation was largest in the weak layer, up to a distance of around $x = 1.6$ m (Figure 8 b3). That the crack propagated to this point was also clearly visible in the $w(t)$ of the DIC subsets in the slab. Indeed, the end displacement ($t > t_b$) of the slab decreased continuously with increasing x until no vertical displacement was observed for $x > 1.6$ m (Figure 8 b1). The horizontal displacement $u(t)$, on the other hand, extended beyond the arrested crack tip (1.6 m $< x <$ 2 m), as expected for a bending slab. Interestingly, for $x < 1.2$ m, $u(t)$ decreased after reaching a maximum value before t_b, suggesting that the slab experienced some support from the disaggregated weak layer and substrate. This recovered support introduced a bending moment, acting in the opposite direction to the bending moment of the free hanging beam end.

3.2. Mechanical properties

Depending on the method, the effective elastic modulus of the slab ranged from 1.3 to 5.4 MPa (Table 2). The SMP-based modulus E_{sl}^{BR} was the average from the 5 measurements along the PST. Using the RW method, the elastic modulus of the weak layer was also estimated at 0.12 MPa.

To verify the robustness of the derived elastic moduli E_{sl}^{VH} and E_{sl}^{RW}, we progressively increased the upper bound of the fit interval r_{max} from 17 cm to r_c (Figure 10a). Values of E_{sl}^{VH} rapidly decreased from 22 MPa to 1.8 MPa for $r_{max} = 25$ cm (orange triangles in Figure 10a). Subsequently, the decrease was much slower, finally reaching a value of 1.3 MPa at r_c. While values of E_{sl}^{RW} were also larger for shorter fit intervals (blue triangles in Figure 10a), the decrease was less pronounced than for E_{sl}^{VH}. Furthermore, E_{sl}^{RW} and E_{wl}^{RW} were very consistent for $r_{max} > 15$ cm (Figure 10 a).

15

Table 2: Effective elastic modulus of the slab and weak layer (E_{sl} and E_{wl}) as well as the weak layer specific fracture energy w_f derived from the VH, RW, and BR method for PST3. For the specific fracture energy w_f we additionally used a power-law fit (FU)

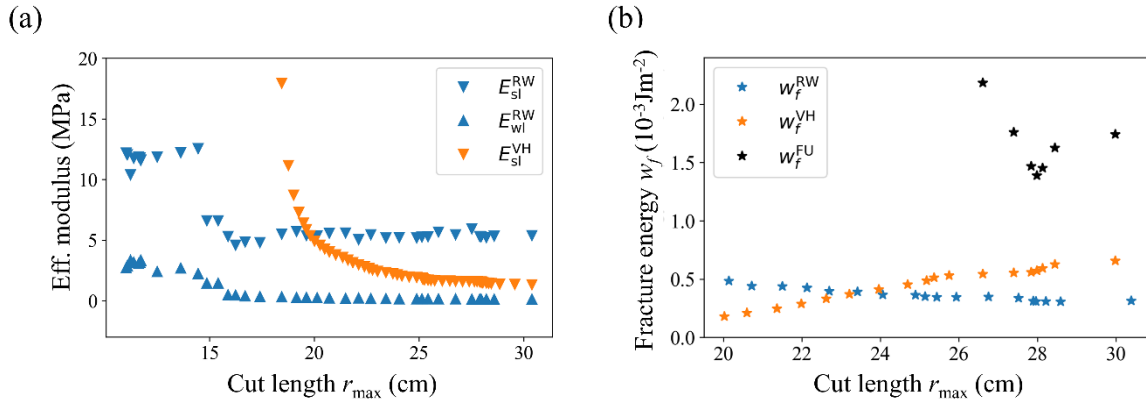|	E_{sl} (MPa)	E_{wl} (MPa)	w_f (J m^{-2})
VH	1.3	-	0.66
RW	5.4	0.12	0.31
BR	2.7	-	0.36
FU	-	-	1.74

(a) (b)

Figure 10: (a) Effective elastic moduli estimated with VH (E_{sl}^{VH}) and RW method (E_{sl}^{RW}, E_{wl}^{RW}) using increasing fitting intervals. (b) Weak layer specific fracture energy estimated with RW method (w_f^{RW}, blue stars), VH method (w_f^{VH}, orange stars) and a power-law fit (w_f^{FU}, black stars) using increasing fitting intervals.

Considering the weak layer specific fracture energy w_f, the BR and the RW estimates were 0.36 and 0.31 Jm^{-2}, respectively, while the VH and FU estimates were higher, 0.66 J m^{-2} and 1.7 J m^{-2}, respectively (Table 2). For the VH, RW and FU method, we quantified the robustness again by checking the trends with increasing cut lengths r (Figure 10b). Of course, to derive w_f both models are evaluated at the critical cut length $r = r_c$, but the computation of w_f is based on E_{sl} (and E_{wl} for the RW method), and E_{sl} is sensitive to changes of the fit interval ($r < r_{max}$, VH method) or when taking another displacement field ($r = r_{max}$, RW method). The spread was largest in w_f^{FU}, and there were opposite trends in w_f^{VH} and w_f^{RW}. Values of w_f^{FU} for $r_{max} < 25$ cm were very large (up to 3000 J m^{-2}) and are not shown in Figure 10b.

3.3. Crack speed and touchdown distance

We used three different methods to estimate the crack speed and its evolution along the PST: the displacement, the strain and the cross-correlation approach. With the displacement and the strain approach the crack tip is located using threshold values, while no threshold is required for cross-correlating the acceleration curves. This similarity in methods is also reflected in the

16

comparable values of c^{disp} and c^{strain} for PST2 and PST3 (blue and green lines in Figure 11). Results obtained with the correlation method, on the other hand, were substantially higher and also followed completely different trends throughout the PST experiments (orange lines in Figure 11).

345 In PST2 the crack did not reach the far end of the column, and crack speed values were only determined up to the crack arrest point ($x = 1.6$ m, Figure 11 b). Overall, mean c^{disp} and c^{strain} values were similar (Table 3) and there was no clear trend throughout the PST (blue and green lines Figure 11a). In contrast, mean c^{corr} was much larger, especially near the edges of the PST. For the PST section between 0.7 and 1.3 m, the speed was rather constant with a mean value of $c^{\text{corr}} = 17.5 \pm 0.6$ m s^{-1}.

Table 3: Mean crack speeds of PST2 and PST3 estimated with the displacement (c^{disp}), strain (c^{strain}) and correlations (c^{corr}) based
350 **method.**

	c^{disp} (m s^{-1})	c^{strain} (m s^{-1})	c^{corr} (m s^{-1})
PST2	9.1 ± 0.9	6.9 ± 2.6	34.5 ± 2.2
PST3	22.2 ± 2.3	17 ± 5	73 ± 11
PST3 (1 m $< x < 2$ m)	24 ± 3	21 ± 5	30.3 ± 1.3

For PST3, c^{disp} and c^{strain} were again comparable and and exhibited a similar trend across the PST. After an initial increase up to about $x = 1$ m, crack speeds remained rather constant throughout the remainder of the PST (blue and green lines in Figure 11b). The values of c^{corr} were again much higher, especially at the beginning and the end of the experiment (Figure 11a, orange line).
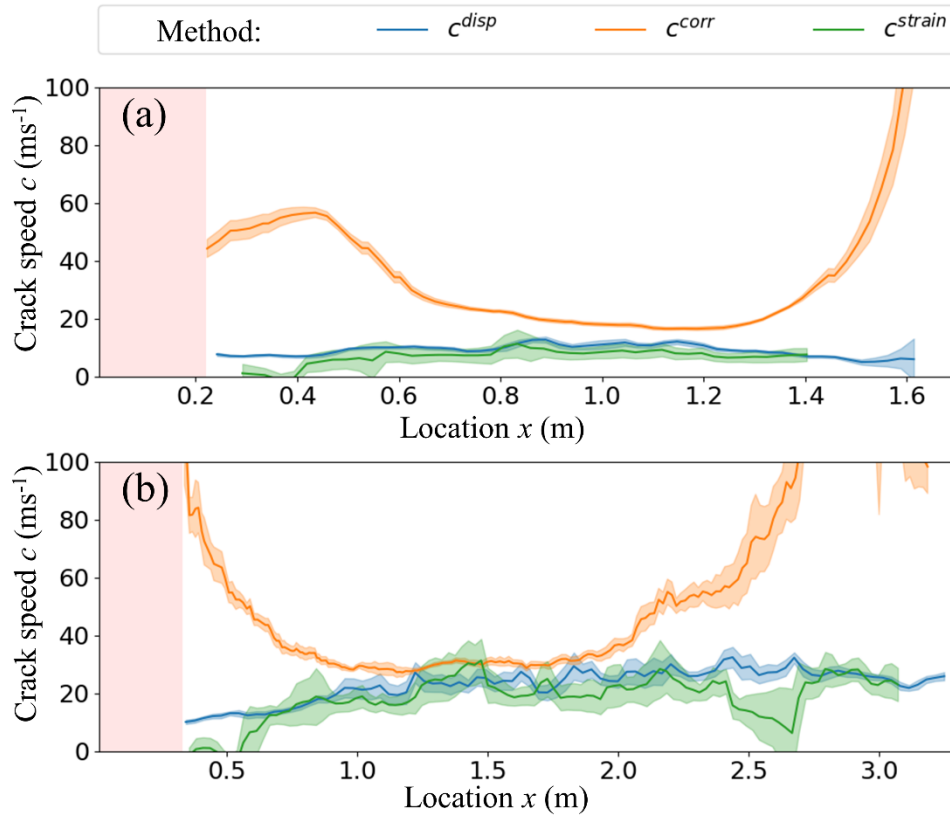
Figure 11: Speed estimates along the beam for (a) PST2 and (b) PST3. The speeds are either based on the displacement (blue curve), the strain (green line) or the correlation method (orange line). The area of the beam that was saw cut ($x < r_c$) is shaded red. The 95% confidence interval was used to indicate the uncertainty and is depicted as a transparent region behind the corresponding lines.

For PST3, we estimated the length of the touchdown distance λ and its evolution along the PST. As DIC subsets at the beginning of the PST beam came to a rest ($\dot{w}(t) < 1.9 \times 10^{-4}$ m s⁻¹) the velocity of DIC subsets at $x = 2.9$ m started exceeding the threshold value, suggesting an initial touchdown distance of 2.9 m. As the crack propagated across the column, λ decreased to around 2.7 m before increasing again towards the far end of the PST (Figure 12). As λ was only somewhat shorter than the column length, we could only evaluate it within the last 40 cm of crack propagation.
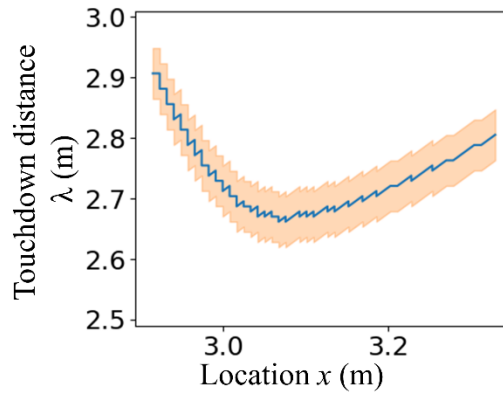
18

Figure 12: Touchdown distance λ in PST3 with crack tip location (blue line). The orange transparent region indicates the uncertainty.

4. DISCUSSION

365 We presented an experimental method to analyse self-sustained crack propagation, i.e. the beginning of dynamic crack propagation, in weak snowpack layers. In this phase, we observed weak layer failure and the associated slab subsidence, in accordance with many previous field studies (van Herwijnen and Birkeland, 2014; van Herwijnen et al., 2016; van Herwijnen and Jamieson, 2005; van Herwijnen et al., 2010). However, in contrast to these previous studies that relied on particle tracking velocimetry (PTV), our use of the DIC method allowed us to observe these processes in much greater detail. For the first time,

370 we were able to measure strain fields in a PST, showing strain concentrations in the area of the weak layer (Figure 8) as well as in the slab in experiments with slab fractures. The high frame rate of our video recording combined with the much higher spatial resolution also allowed us to obtain detailed insights into changes in crack speed and touchdown distance during crack propagation.

When observing a PST experiment in the field, it is often very difficult to determine the exact location of crack arrest,

375 distinguish between crack arrest far away from r_c and full propagation, or determine whether a slab fracture occurred when the crack arrested. The unusual results obtained for PST3, where full crack propagation occurred, followed by a secondary fracture in a different weak layer, were not recognized in the field. With PTV, the method used in previous studies to investigate crack propagation in PSTs, the interpretation of the observed differences in the displacement curves would be ambiguous (Figure 8, c1 to c3). However, the strain field obtained with DIC clearly highlighted the presence of the secondary crack propagating in

380 the opposite direction in a weak snow layer, consisting of precipitation particles closer to the snow surface. This secondary fracture was very likely triggered by the sudden drop of the slab after the crack had propagated through the tested weak layer. The secondary crack was stopped by two slab fractures (Supplement A). These results clearly highlight the advantages of DIC to investigate intricate subtleties occurring in PST experiments and resolve the processes during crack propagation in great detail.

19

385 Despite the increased detail obtained with DIC, it was not possible to measure absolute values of strain in the weak layer. The DIC subset size ($\approx$ 3 cm) was still larger than the vertical extent of the weak layer ($\approx$ 1.5 cm). Values of strain should thus be considered as an average strain over an area with high strain occurring in the weak layer and areas with rigid body motion (portion of the slab, visible in the DIC subset) or even areas without motion (portion of the substrate). Reducing the field of view of the camera would increase spatial measurement resolution, thus by taking close-ups of the weak layer it is theoretically

390 possible to reduce the DIC subset size to less than the extent of the weak layer. However, snow is a porous material consisting of interconnected ice crystals and the thickness of surface hoar layers is often on the same spatial scale as individual crystals. Therefore, the concept of a continuum strain in the weak layer does not exist at this scale, since strain distribution is locally very heterogeneous within the ice matrix. In addition, an appropriate speckling of the measuring surface then becomes difficult, as single crystals would have to be speckled. The strain measurements obtained with DIC therefore show strain localization

395 indicative of crack formation and propagation, but cannot be used to accurately quantify the exact deformation behaviour within the weak layer.

4.1. Crack speed and touchdown distance

Thanks to the high frame rates of our recordings, we were able to calculate derivatives of the displacements to obtain speed and acceleration of the DIC subsets. In the past, crack speed and touchdown distance were estimated solely based on

400 displacement data (Bair et al., 2014; van Herwijnen and Jamieson, 2005; van Herwijnen et al., 2010). Here, we exploited speed and acceleration data to derive additional estimates of crack speed and touchdown distance. To estimate these quantities, the position of the crack tip must be known at all times. For opening cracks, the position of the crack tip is the place where the material separates. For closing cracks, as is the case in our experiments, no generally valid definition exists. We therefore evaluated different methods to estimate crack propagation speed.

405 We attribute differences in crack speeds obtained in the experiments to the dynamics of crack propagation. With crack extension the load type, strain rate and boundary conditions change, affecting crack growth itself. Slab displacements of DIC subsets, and thus all the variables derived from it, such as speed and acceleration, therefore changed during crack propagation. For instance, in Figure 8a and 9b the shape of the displacement curves changes along the PST. The various methods used to estimate crack speed were influenced by different aspects of this change in shape. For example, c^{disp} is sensitive to how rapidly

410 displacement curves initially increase to the threshold value. The correlation method, however, is very sensitive to small changes in the shape of the entire displacement curve, in particular changes in curvature. These shape changes were most pronounced near both ends of the PST, as boundary conditions change resulting in edge effects (Bair et al., 2014). Hence, in the absence of steady-state crack propagation, the different methods will yield different results.

Looking more closely at the drivers of crack propagation dynamics, two effects can be distinguished. First at the saw end

415 where crack propagation begins, the free-hanging section of the slab steadily grows as long as the slab does not rest on the crushed weak layer. This changes the magnitude and the angle of loading at the location of the crack tip. Second, as the crack approaches the far end of the beam, there are again changes in the magnitude and loading angle at the crack tip as the bending

20

moment in the slab is forced to zero (free boundary). These changes affect the shape of the displacement curves and thus crack speed estimates. In the middle section of the PST, edge effects are less pronounced. Here, possible drivers for crack propagation

420   dynamics are strain rate effects and smaller geometric changes, e.g. changes in touchdown distance. Nevertheless, as long as there is no steady-state crack propagation, slab displacement curves change along the PST column (increasing x-location). These changes provide an explanation for the offset observed in the crack speed estimates (Figure 11). Very long PST experiments would therefore be needed to clarify the existence of steady-state crack propagation (Heierli, 2005). In such experiments, the two prominent dynamical effects (close to column ends and far from column ends) should be more clearly

425   separated. This should allow for measurements of constant crack speed far from the column edges, no matter which method is applied. In our experiments, c^{corr} was very sensitive to changes in the propagation dynamics, suggesting it is more suited to highlight edge effects rather than estimating reliable crack speed values. Crack speed estimates of c^{strain} and c^{disp} were similar and robust, suggesting that these methods are better suited to estimate crack propagation speeds in PSTs.

While we did not observe steady-state crack propagation within our PSTs, the crack speed values in PST3 can nonetheless be

430   compared with theoretical predictions. Heierli (2005) formulated simple expressions for the crack propagation speed and wavelength of a steady-state collapse wave. With this model, we obtained a wavelength of 2.7 m travelling at a speed of 35 m s^{-1}. The crack speed values around the middle of the PST (1 m < x < 2 m) ranged from 21 to 30 m s^{-1} (Table 3), somewhat lower than those predicted by the model for steady-state crack propagation. The predicted wavelength and the observed touchdown distance were, however, in good agreement (Figure 12). To date, only Bair et al. (2014) reported touchdown

435   distances, and these were much longer than those predicted by theory. They attributed the discrepancy mostly to the model assumption, namely that the slab is in free fall motion during weak layer collapse. Due to experimental limitations, Bair et al. (2014) could not verify this assumption. In our experiments, however, slab accelerations never exceeded 3 m s^{-2} (Figure 5) clearly showing that the slab is not in free fall (Video A1 in the Supplement).

As a practical implication, our results emphasize the need to revisit the predictive power of normal-sized PST experiments.

440   That the measured touchdown distance is longer than the typical PST column length once more shows that normal-sized PSTs cannot be used to assess the propensity for self-sustained crack propagation.

4.2.   Elastic modulus and weak layer specific energy

In our study, all estimates of slab effective modulus were of the same order of magnitude (Table 2). The ratios were approximately $E_{\mathrm{sl}}^{\mathrm{VH}} \approx \frac{1}{2} E_{\mathrm{sl}}^{\mathrm{BR}} \approx \frac{1}{4} E_{\mathrm{sl}}^{\mathrm{RW}}$. Comparing the moduli derived from the displacement fields, we consider those

445   obtained with the RW method as the most appropriate, as these were more stable with increasing cut lengths (Figure 10a) and visually the experimental data and the modelled displacements seem to agree very well (Figure 3). Moreover, with the RW method the elastic modulus of the weak layer can be estimated under the assumptions of isotropy.

For the weak layer specific fracture energy, results were also of the same order of magnitude, although the differences were somewhat larger ($w_f^{\mathrm{RW}} \approx w_f^{\mathrm{BR}} \approx 1/2\, w_f^{\mathrm{VH}} \approx 1/5\, w_f^{\mathrm{FU}}$). As the formulation of Heierli et al. (2008a) only provided a fair fit

450   to the data (orange line in Figure 3a), we also fitted a power-law function to the data, resulting into a 2.5 times larger value of fracture energy. The fracture energy estimates from the SMP data were lower than the VH and FU values. However, the w_f^{BR} are considered less reliable as these were obtained using a parameterization based on data obtained with a method very similar to the VH method (Equation 4). Nevertheless, as the SMP is an efficient instrument to rapidly and objectively measure snowpack parameters in the field, we believe that a comparison with more elaborate methods to estimate specific fracture

455   energy is warranted, and may lead to a new parameterization for SMP data.

    The RW method provided lower estimates of the specific fracture energy as the VH and FU method. This might in part be due to limitations of the RW model. Currently, the weak layer in the model can be conceptualized as a set of smeared springs attached to the midsurface of a homogeneous slab. While this reduces the effort of solving the governing equations, the disadvantage is that the mode II energy release rate G_{II} in flat field PSTs is always zero as $u_{\mathrm{RW}}(x = r_c, z = z_{\mathrm{wl}})$ is zero (cf.

460   Equation 3 and bottom right in Figure 3b). One remedy would be to couple the weak layer to the bottom of the slab to determine mode II specific fracture energies from flat field experiments as well. Having estimates for both of these independent weak layer material properties would be of interest to better describe mode mixety in weak layer crack propagation.

    Overall, the differences in fracture energy estimates clearly highlight that we are not yet able to reliably measure this important material property in snow, beyond order of magnitude estimates. Future research should therefore focus on designing tailored

465   field or laboratory experiments to independently measure weak layer fracture energies to validate existing methods.

5.   CONCLUSIONS

We recorded PST experiments using a portable high-speed camera. By applying a speckling pattern on the entire sidewall of a PST column, we then used digital image correlation (DIC) to derive the displacement and strain of the slab, and the strain across the weak layer.

470 From displacement and strain fields we derived two independent estimates of crack speed (24 ± 3 m s^{-1} and 21 ± 5m s^{-1}). In addition, we computed crack speeds by correlating the downward acceleration of the slab in time (30.3 ± 1.3 m s^{-1}). Our results suggest that crack speed can reliably be derived with both threshold-based approaches as these values were in good agreement. Values obtained with the correlation-based technique were, however, susceptible to changes in the shape of the displacement curves and hence to edge effects in the PST. Therefore, values from the correlation-based technique resulted in larger variations

475 in speed along the PST. In general, with our measurement setup and analyses, changes in crack propagation speed at the scale of a PST beam can be investigated.

From the downward velocity field of the slab we estimated the touchdown distance (2.7 m) and its change during crack propagation in a PST. Our results are in good agreement with theoretical predictions from a solitary wave model. However, the model assumption, that the slab is in free fall behind the crack tip was refuted based on the observed slab acceleration.

480 Crack speed and touchdown distance were both affected by edge effects on both free edges of the PST. Our results suggest that much longer PST experiments are required to study the propensity of sustained crack propagation.

While we measured the evolution of strain over the weak layer during crack propagation, it was not possible to determine the true strain within the weak layer due to experimental limitations. The spatial resolution is still too low, since one DIC subset incorporates slab or substrate regions adjacent to the weak layer. In the future, we plan to increase the spatial resolution by filming close-ups around the weak layer, even though a measurement of true strain within the weak layer will probably not be feasible.

Nevertheless, the increased spatial resolution of our DIC setup offered an alternative method for deriving the effective elastic modulus of the slab from the displacement field. Compared to already established methods, the method based on the model presented by Rosendahl and Weissgraeber (2020) provided a more robust estimate of the effective elastic modulus of the slab and, in addition, of the weak layer.

Finally, we also computed weak layer specific fracture energy. The large variability in our results ($0.31 - 1.74$ J m^{-2}) highlight that there is still a need to establish a physically sound and specifically tailored method for measuring weak layer fracture energy.

Overall, this study demonstrates the great potential of the experimental setup and DIC based analysis methods that in the future should allow for a deeper understanding of the dynamics of crack propagation at the slope scale, which ultimately determines avalanche size.

References

Alfarah, B., López-Almansa, F., and Oller, S.: New methodology for calculating damage variables evolution in Plastic Damage Model for RC structures, Eng. Struct., 132, 70-86, https://doi.org/10.1016/j.engstruct.2016.11.022, 2017.

515   Bair, E. H., Simenhois, R., van Herwijnen, A., and Birkeland, K.: The influence of edge effects on crack propagation in snow stability tests, Cryosphere, 8, 1407-1418, https://doi.org/10.5194/tc-8-1407-2014, 2014.

Bradski, G., and Kaehler, A.: Learning OpenCV, O'Reilly Media Inc., Sebastopol, 2008.

Broberg, K. B.: How fast can a crack go?, Materials Science, 32, 80-86, https://doi.org/10.1007/BF02538928, 1996.

Fierz, C., Armstrong, R. L., Durand , Y., Etchevers, P., Greene, E., McClung, D. M., Nishimura, K., Satyawali, P. K., and Sokratov, S. A.: The International Classification for Seasonal Snow on the Ground, HP-VII Technical Documents in Hydrology, IACS Contribution No 1, UNESCO-IHP, Paris, France, 90 pp., 2009.

520

Gauthier, D., and Jamieson, J. B.: Evaluating a prototype field test for weak layer fracture and failure propagation, Proceedings ISSW 2006. International Snow Science Workshop, Telluride CO, U.S.A., 1-6 October 2006, 107-116, 2006a.

Gauthier, D., and Jamieson, J. B.: Towards a field test for fracture propagation propensity in weak snowpack layers, J. Glaciol., 52, 164-168, https://doi.org/10.3189/172756506781828962, 2006b.

525   Greene, E., Birkeland, K., Elder, K., McCammon, I., Staples, M., and Sharaf, D.: Snow, Weather, and Avalanches: Observation Guidelines for Avalanche Programs in the United States, 3rd ed., American Avalanche Association, Victor ID, U.S.A., 104 pp., 2016.

Gross, D., and Seelig, T.: Bruchmechanik, 3rd ed., Springer, Berlin, Germany, 317 pp., 2001.

Heierli, J.: Solitary fracture waves in metastable snow stratifications, J. Geophys. Res., 110, F02008, https://doi.org/10.1029/2004JF000178, 2005.

530   Heierli, J.: Anticrack model for slab avalanche release, Ph.D., University of Karlsruhe, Karlsruhe, Germany, 102 pp., 2008.

Heierli, J., Gumbsch, P., and Zaiser, M.: Anticrack nucleation as triggering mechanism for snow slab avalanches, Science, 321, 240-243, https://doi.org/10.1126/science.1153948, 2008a.

Heierli, J., van Herwijnen, A., Gumbsch, P., and Zaiser, M.: Anticracks: A new theory of fracture initiation and fracture propagation in snow, Proceedings ISSW 2008, International Snow Science Workshop, Whistler, Canada, 21-27 September 2008, 2008b.

535   Heierli, J., Gumbsch, P., and Sherman, D.: Anticrack-type fracture in brittle foam under compressive stress, Scr. Mater., 67, 96-99, https://doi.org/10.1016/j.scriptamat.2012.03.032, 2012.

Jamieson, J. B., and Johnston, C. D.: A fracture-arrest model for unconfined dry slab avalanches, Can. Geotech. J., 29, 61-66, https://doi.org/10.1139/t92-007, 1992.

Johnson, J. B.: A statistical micromechanical theory of cone penetration in granular materials, U.S. Army Corps of Engineers, Engineer Research and Development Center, Hanover NH, U.S.A., ERDC/CRREL Technical Report, ERDC/CRREL-TR-03-3, 32, 2003.

540

Löwe, H., and van Herwijnen, A.: A Poisson shot noise model for micro-penetration of snow, Cold Reg. Sci. Technol., 70, 62-70, https://doi.org/10.1016/j.coldregions.2011.09.001, 2012.

Marshall, H.-P., and Johnson, J. B.: Accurate inversion of high-resolution snow penetrometer signals for microstructural and micromechanical properties, J. Geophys. Res., 114, F04016, https://doi.org/10.1029/2009jf001269, 2009.

545   McClung, D. M.: Approximate estimates of fracture speeds for dry slab avalanches, Geophys. Res. Lett., 32, L08406, https://doi.org/10.1029/2005GL022391, 2005.

McClung, D. M., and Schaerer, P.: The Avalanche Handbook, 3rd ed., The Mountaineers Books, Seattle WA, U.S.A., 342 pp., 2006.

Pudasaini, S. P., and Hutter, K.: Avalanche dynamics: Dynamics of rapid flows of dense granular avalanches, Springer, Berlin, Heidelberg, Germany, 602 pp., 2007.

550   Reuter, B., Schweizer, J., and van Herwijnen, A.: A process-based approach to estimate point snow instability, Cryosphere, 9, 837-847, https://doi.org/10.5194/tc-9-837-2015, 2015.

Reuter, B., and Schweizer, J.: Describing snow instability by failure initiation, crack propagation, and slab tensile support, Geophys. Res. Lett., 45, 7019-7027, https://doi.org/10.1029/2018GL078069, 2018.

Reuter, B., Proksch, M., Löwe, H., van Herwijnen, A., and Schweizer, J.: Comparing measurements of snow mechanical properties relevant for slab avalanche release, J. Glaciol., 65, 55-67, https://doi.org/10.1017/jog.2018.93, 2019.

555

Rosendahl, P. L., and Weissgraeber, P.: Modeling snow slab avalanches caused by weak-layer failure - Part 1: Slabs on compliant and collapsible weak layers, Cryosphere, 14, 115-130, https://doi.org/10.5194/tc-14-115-2020, 2020.

Schneebeli, M., and Johnson, J. B.: A constant-speed penetrometer for high-resolution snow stratigraphy, Ann. Glaciol., 26, 107-111, https://doi.org/10.3198/1998AoG26-1-107-111, 1998.

560   Schweizer, J., Jamieson, J. B., and Schneebeli, M.: Snow avalanche formation, Rev. Geophys., 41, 1016, https://doi.org/10.1029/2002RG000123, 2003.

Schweizer, J., van Herwijnen, A., and Reuter, B.: Measurements of weak layer fracture energy, Cold Reg. Sci. Technol., 69, 139-144, https://doi.org/10.1016/j.coldregions.2011.06.004, 2011.

565 Schweizer, J., Bartelt, P., and van Herwijnen, A.: Snow avalanches, in: Snow and Ice-Related Hazards, Risks, and Disasters, 2nd ed., edited by: Haeberli, W., and Whiteman, C., Elsevier, Amsterdam, Netherlands, 377-416, 2021.

Sigrist, C., Schweizer, J., Schindler, H. J., and Dual, J.: On size and shape effects in snow fracture toughness measurements, Cold Reg. Sci. Technol., 43, 24-35, https://doi.org/10.1016/j.coldregions.2005.05.001, 2005.

Sigrist, C., Schweizer, J., Schindler, H. J., and Dual, J.: Measurement of fracture mechanical properties of snow and application to dry snow slab avalanche release, Geophys. Res. Abstr., 8, 08760, 2006.

570 Sigrist, C., and Schweizer, J.: Critical energy release rates of weak snowpack layers determined in field experiments, Geophys. Res. Lett., 34, L03502, https://doi.org/10.1029/2006GL028576, 2007.

Turner, D. Z.: Digital Image Correlation Engine (DICe) Reference Manual, National Technology & Engineering Solutions of SandiaSAND2015-10606 O, 2015.

van Herwijnen, A., and Jamieson, B.: High-speed photography of fractures in weak snowpack layers, Cold Reg. Sci. Technol., 43, 71-82, https://doi.org/10.1016/j.coldregions.2005.05.005, 2005.

575

van Herwijnen, A., and Heierli, J.: In-situ measurement of the mechanical energy associated with crack growth in weak snowpack layers and determination of the fracture energy, Geophys. Res. Abstr., 12, 11743, 2010.

van Herwijnen, A.: Experimental analysis of snow micropenetrometer (SMP) cone penetration in homogeneous snow layers, Can. Geotech. J., 50, 1044-1054, https://doi.org/10.1139/cgj-2012-0336, 2013.

580 van Herwijnen, A., and Birkeland, K. W.: Measurements of snow slab displacement in Extended Column Tests and comparison with Propagation Saw Tests, Cold Reg. Sci. Technol., 97, 97-103, https://doi.org/10.1016/j.coldregions.2013.07.002, 2014.

van Herwijnen, A., Gaume, J., Bair, E. H., Reuter, B., Birkeland, K. W., and Schweizer, J.: Estimating the effective elastic modulus and specific fracture energy of snowpack layers from field experiments, J. Glaciol., 62, 997-1007, https://doi.org/10.1017/jog.2016.90, 2016.

585 Virtanen, P., Gommers, R., Oliphant, T. E., Haberland, M., Reddy, T., Cournapeau, D., Burovski, E., Peterson, P., Weckesser, W., Bright, J., van der Walt, S. J., Brett, M., Wilson, J., Millman, K. J., Mayorov, N., Nelson, A. R. J., Jones, E., Kern, R., Larson, E., Carey, C. J., Polat, İ., Feng, Y., Moore, E. W., VanderPlas, J., Laxalde, D., Perktold, J., Cimrman, R., Henriksen, I., Quintero, E. A., Harris, C. R., Archibald, A. M., Ribeiro, A. H., Pedregosa, F., van Mulbregt, P., Vijaykumar, A., Bardelli, A. P., Rothberg, A., Hilboll, A., Kloeckner, A., Scopatz, A., Lee, A., Rokem, A., Woods, C. N., Fulton, C., Masson, C., Häggström, C., Fitzgerald, C.,
590 Nicholson, D. A., Hagen, D. R., Pasechnik, D. V., Olivetti, E., Martin, E., Wieser, E., Silva, F., Lenders, F., Wilhelm, F., Young, G., Price, G. A., Ingold, G.-L., Allen, G. E., Lee, G. R., Audren, H., Probst, I., Dietrich, J. P., Silterra, J., Webber, J. T., Slavič, J., Nothman, J., Buchner, J., Kulick, J., Schönberger, J. L., de Miranda Cardoso, J. V., Reimer, J., Harrington, J., Rodríguez, J. L. C., Nunez-Iglesias, J., Kuczynski, J., Tritz, K., Thoma, M., Newville, M., Kümmerer, M., Bolingbroke, M., Tartre, M., Pak, M., Smith, N. J., Nowaczyk, N., Shebanov, N., Pavlyk, O., Brodtkorb, P. A., Lee, P., McGibbon, R. T., Feldbauer, R., Lewis, S., Tygier, S.,
595 Sievert, S., Vigna, S., Peterson, S., More, S., Pudlik, T., Oshima, T., Pingel, T. J., Robitaille, T. P., Spura, T., Jones, T. R., Cera, T., Leslie, T., Zito, T., Krauss, T., Upadhyay, U., Halchenko, Y. O., and Vázquez-Baeza, Y.: SciPy 1.0: fundamental algorithms for scientific computing in Python, Nature Methods, 17, 261-272, https://doi.org/10.1038/s41592-019-0686-2, 2020.

Walters, D. J., and Adams, E. E.: Quantifying anisotropy from experimental testing of radiation recrystallized snow layers, Cold Reg. Sci. Technol., 97, 72-80, https://doi.org/10.1016/j.coldregions.2013.09.014, 2014.

600